Extreme Mechanics Letters 40 (2020) 100912

Contents lists available at ScienceDirect

Extreme Mechanics Letters

journal homepage: www.elsevier.com/locate/eml

# 3D kirigami metamaterials with coded thermal expansion properties

Nan Yang [a,*], Mingkai Zhang [b], Rui Zhu [b,*]

[a] Intelligent Manufacturing Key Laboratory of Ministry of Education, Shantou University, Shantou 515063, China
[b] Key Laboratory of Dynamics and Control of Flight Vehicle, Ministry of Education, School of Aerospace Engineering, Beijing Institute of Technology, Beijing, 100081, China

ARTICLE INFO

*Article history:*
Received 18 May 2020
Received in revised form 30 July 2020
Accepted 30 July 2020
Available online 4 August 2020

*Keywords:*
Coded thermal expansions
3D mechanical metamaterials
Kirigami
Negative Poisson's ratio
Shape memory alloy

ABSTRACT

Capability of achieving desired thermal expansions is critically important for various engineering applications. Inspired by the morphable kirigami patterns, three-dimensional (3D) mechanical metamaterials are designed and fabricated with their effective thermal expansion properties being coded within the fundamental thermo-mechanical coupled microstructures. With the concept of 'bit' being introduced in the basic quarter unit, we construct ring-like unit cells which are assembled to form different 2D and 3D metamaterials with programmable elastic deformations upon changes in temperature. Both simulations and experiments are performed at different levels of the architectured materials indicating that the targeted isotropic and anisotropic deformations can be achieved in a large range (from -40% to 10% strain). Finally, the positively correlated relation between thermal expansion property and Poisson's ratio is also discussed. This work opens up new avenues for potential mechanical metamaterial applications in deformable electronics, self-folding materials, artificial muscles, and robotics.



On many occasions, we require materials that can achieve targeted size variations in response to temperature changes, for example, space crafts, buildings, solar energy systems, lens, engines and artificial muscles [1–6]. These size changes induced by temperature can provide power (such as artificial muscles), efficiently utilize energy (solar energy systems) and adapt the thermal working environments (tooth fillings and piping connections). Under these requirements, there have been two main approaches based on naturally grown materials and artificially engineered structures to alter the overall thermal expansion properties of the system and therefore, achieve the desired thermal deformations. For the natural materials-based approach, although chemical reactions can be used to promote the materials with tunable thermal expansion [7–10], the material's intrinsic framework at the molecular level prevents any extreme modifications which limits their applications. Further adjustments of the thermal expansion based on supramolecular mechanisms [4] include low-frequency phonon modes, magnetostrictive, ferroelectric and displacive phase transitions. However, the materials treated by these methods cannot be robust and durable over large temperature changes [11]. The artificial structures, on the other hand, are engineered with microstructures functioning as man-made atoms [12] which can provide customized overall mechanical [13] and thermal properties [14–22].

Recent research on kirigami/origami reveals that the art for paper cutting/folding can also efficiently guide the microstructure designs of artificial metamaterials with peculiar macroscopic mechanical properties, such as negative Poisson's ratio [23–25], negative stiffness [26], adjustable curvature [27] and multistability [28,29]. These origami-inspired designs also prove to be advantageous in tuning the thermal expansion of metamaterials. Boatti et al. [11] combined the well-known Miura-ori pattern with bilayer facets and demonstrated a wide range of thermal expansion coefficients in the 2D metamaterial. The non-cut pattern prevents the formation of complicated 3D tessellation which possesses more degrees of freedom for thermo-mechanical coupling and even reprogramming.

In this work, we design and fabricate 3D kirigami metamaterials with thermo-mechanical coupled microstructures which enable the metamaterials to possess multiple thermal deformation modes as well as large strains. The core part of the microstructure is a new kirigami pattern with '$\gamma$'-shaped shape memory alloy (SMA) sheets/patches positioned at the dihedrals. The deformation of the proposed metamaterial is actually controlled by two mechanisms: the shape memory effect, as a local deformation mechanism, and the kirigami morphology, as a global deformation mechanism. Specifically, the '$\gamma$'-shaped SMA patch controls the local deformation angle ($\theta$) (see Fig. S12), which changes the shape of the individual kirigami unit cell and therefore, contributes to the global deformation of the metamaterial via the different assembling methods of multiple unit cells. Furthermore,

* Corresponding authors.
*E-mail addresses:* nyang@stu.edu.cn (N. Yang), ruizhu@bit.edu.cn (R. Zhu).

https://doi.org/10.1016/j.eml.2020.100912
2352-4316/

with the concept of 'bit' being introduced in the microstructure, a ring-like unit cell is formed with multiple bits and becomes the building brick to construct 2D and 3D metamaterials with coded deformation modes upon corresponding temperature changes.

## 1. Unit geometry

Two plane angles ($\alpha, \beta$) and three lengths ($q$, $n$, $m$) determine the 2D folding/cutting pattern of 1/4 unit (Fig. 1a, red: mountain creases, blue: valley creases), and four deformation angles ($\theta_1, \theta_2, \theta_3, \theta_4$) determine its 3D configuration (connecting the yellow sides to form new creases). The states of $N$ deformation angles correspond to $N$ 'bits' (as an example here $N = 4$). Assuming the 3D structure as a mechanism with rigid facets and joints (creases), we define $\theta_i < 180°$ as '1' state and $\theta_i > 180°$ as '0' state. In Fig. 1b, each two adjacent bits can be switched between four combinations via point E (initial structure with $\theta_{i-1} = \theta_i = 180°$, non-'0' and non-'1' state). Such structure with two bits can be switched from point A ($\theta_{i-1} < 180°, \theta_i > 180°$, state '1,0') through E to B ($\theta_{i-1} > 180°, \theta_i < 180°$, state '0,1') along the line $\theta_{i-1} + \theta_i = 360°$. It can also be switched from point C ($\theta_{i-1} < 180°, \theta_i < 180°$, state '1,1') through E to D ($\theta_{i-1} > 180°, \theta_i > 180°$, state '0,0') along the line $\theta_{i-1} = \theta_i$. In Fig. 1c, planes ABC and A′B′C′ of a quarter unit are parallel during deformation regardless of patterns, which provides a way to define the sizes in three directions. A ring-like unit is formed by connecting four quarter units with the yellow panels (Fig. 1d). Fig. 1e shows size definition of a ring-like unit following the definition fashion of quarter unit, and the connecting panels can be outward or inward which can be flexibly chosen for the geometrical compatibility with multiple units. 2D cellular structure can be made by combining multiple ring-like units (3 × 3 units with contraction, Fig. 1f). The quarter unit with 4 bits possesses 16 patterns (Fig. 1g). But there are five kinds of deformation behaviors along $Y$-axis ($y/y_0 - \theta$ plot, five colors) and one deformation along $X$-axis ($x/x_0 - \theta$ plot), where $x, y$ denote the sizes along the two directions (see also Fig. 1c), and $x_0, y_0$ denote the initial sizes (with $\theta_i = 180°$, $i = 1 \sim 4$, see also structure E in Fig. 1b), and $\theta$ denotes the deformation angle in '0' pattern bit thus $180° < \theta < 360°$ (for the mode without '0' pattern bits, e.g., '1111', angle $\theta$ is calculated as 360° minus the angle of '1' pattern bit to compare all data in one plot). Therefore, the different deformations along $Y$-axis of a quarter unit contribute many deformation modes for a ring-like unit.

To fabricate ring-like unit samples, thick papers with Young's modulus being 2 GPa are first cut by laser cutter. Then, $\gamma$-shaped TiNi SMA patches, which are fabricated by welding two flat patches (Young's modulus: 100 GPa, thickness: 0.25 mm, length: 14 mm, welded part: 4 mm, width: 6 mm, curvature: 0.05 mm$^{-1}$), are glued on the facets to control the key deformation angle $\theta_i$, as shown in Fig. 1h. A SMA sheet inward or outward the unit denotes '0' or '1' pattern, respectively. The gluing protocol is a soft material and only a very thin layer was applied between the SMA sheet and the thick paper facet. Therefore, its influence on the key deformation angle ($\theta$) and the overall thermal–mechanical behavior can be neglected. When heated, the opening angle ($\delta$, see Fig. S7) of the $\gamma$-SMA patch decreases to actuate each deformation angle $\theta_i$ in the ring-like unit, and the X- and Y-size variation with time of the structure are measured by a camera. The initial values of $\theta$ and $\delta$ are set at 180°, which can be tuned by mechanically adjusting the opening angle $\delta$ before it being heated up. The details of unit geometry, fabrication, deformation measurement and the relation between temperature and deformation for SMA sheet can be found in the Supplementary Materials.

## 2. 2D coded thermal expansions

Interestingly, the coded thermal expansion of a quarter unit makes isotropic and anisotropic deformations for the ring-like units under corresponding temperature changes. In Fig. 2, four quarter units are set in the same pattern (111, 110, 100, or 000), then four isotropic patterns of the ring-like unit are formed. Four different thermal deformation behaviors can be found for each pattern. In Fig. 2a, pattern 111 and 000 show deformation behaviors of full thermal expansion and contraction, respectively. During heating process, patterns 100 and 110 show medium deformations between them. This can be also demonstrated in the experimentally measured results, as shown in Fig. 2b (see deformation photographs in Fig. 2c). See also Supplementary Videos 1∼4, 8 for isotropic deformation.

In Fig. 2b, the structure strain in '111' pattern stops changing within 120 s, while the change in '000' pattern needs more response time. This difference mainly comes from the number of '0' bit. A '0' bit means that a $\gamma$-shaped SMA sheet is fixed inward the structure, so when the structure is self-folded, the outcrop part of the $\gamma$-shaped SMA sheet will conflict with the structure's inner facet and then, prevents the structure from deforming normally (in a much slower manner and then with a hard stop). Eventually, the delay of the strain's converging to constant is observed in the overall response of the metamaterial's unit. On the contrary, the $\gamma$-shaped SMA sheet will not conflict with any part of the structure with '1' bit, so the unit with kirigami structure in '111' pattern deforms normally with its strain converging to a constant value after two minutes of heating.

On the other hand, when the four quarter units are set in different patterns (e.g., pattern #1: 100-000-100-000), as shown in Fig. 3a, the ring-like unit possesses an anisotropic deformation behavior along X and Y direction during heat. In the upper plots in Fig. 3, we can see contractions along both X and Y direction for pattern #1 (Fig. 3a), contraction along Y direction (gray) and slight deformation along X direction (red) for pattern #2 (Fig. 3b), and contraction along Y direction (gray) and expansion along X direction (red) for pattern #3 (Fig. 3c). As evidences, the experimental results and photographs can be seen below the simulation results. See also Supplementary Videos 5∼7.

In Fig. 3b, the simulation of strain indicates expansion along X direction, which is indeed different from the experimental result. The strain results obtained from the simulation (upper part in Fig. 3b) are based on the assumption that the structure facets are rigid and therefore, easy to be kept in symmetric shapes during the structure's deformation. However, the fabricated structure facets in the experiment are soft and bendable, which makes them hard to be kept in perfectly symmetric shapes during the structure's deformations. Consequently, a small perturbation (such as friction between facets and SMA sheets or different responses to heat for different SMA sheets) can break the symmetric assumption and results in different structure's strain responses. When the overall structure's strain changes dramatically, as shown in the red curve of Fig. 3a and the initial part of the red curve of Fig. 3c, the differences between the simulation and experimental results are not obvious. But if the overall structure's strain changes slightly, as shown in the almost flat red curve in Fig. 3b, the unsymmetric facets can cause relatively obvious differences (from slight expansion to slight compression) between the simulation and experimental results.

The thermal expansion coefficients of the ring-like structure coupled with SMA patches can be tuned larger than that of the layered ruthenate [7] and bilayer Miura-ori [11]. But it is not a fair comparison, since the thermal expansion coefficients of the materials used there are very small. In order to compare our work with others in terms of creating artificial architected materials

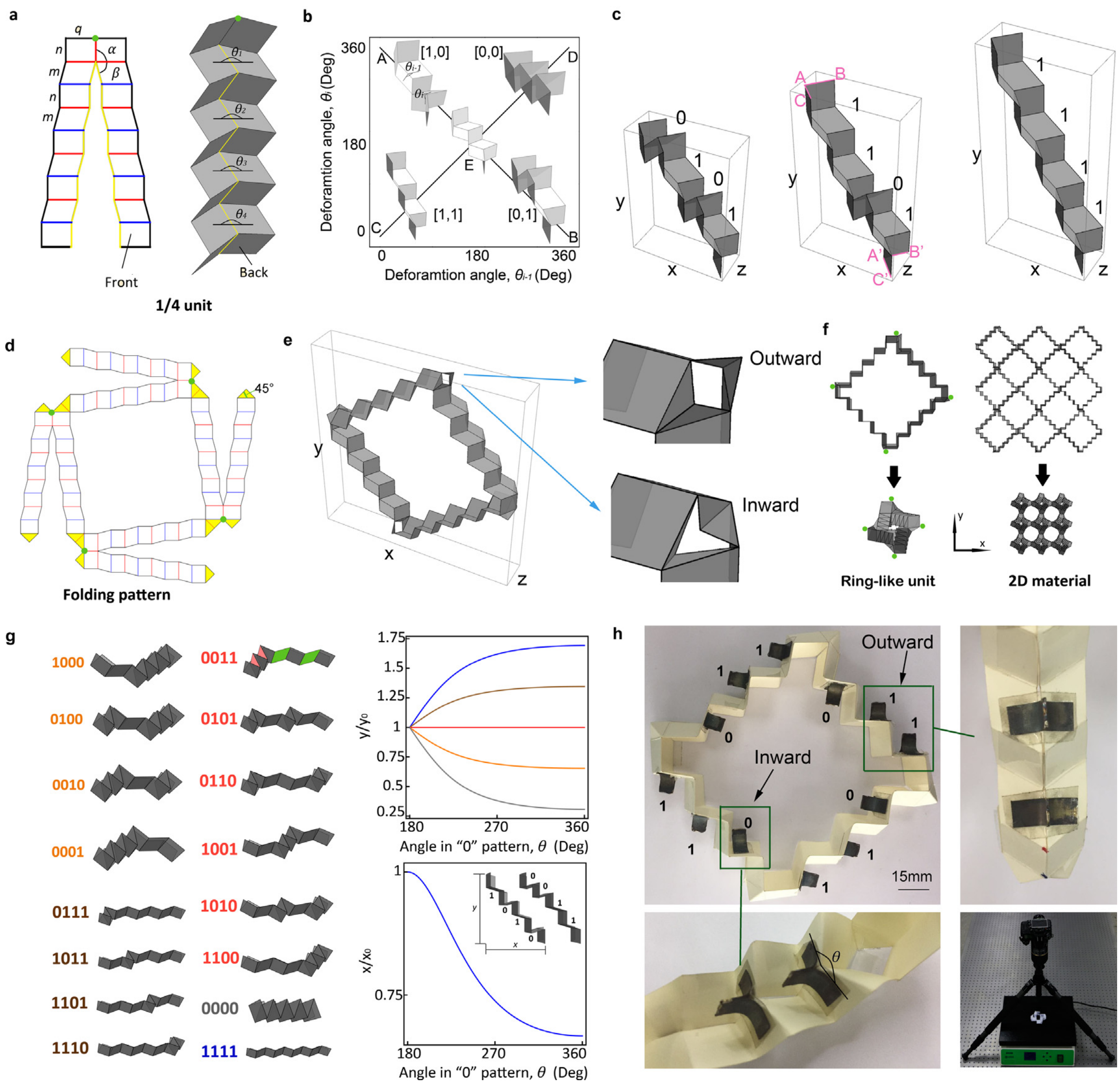


**Fig. 1.** Ring-like unit cell and its 1/4 unit. a, 2D folding pattern and 3D configuration of 1/4 unit. b, Adjacent deformation angles ($\theta_{i-1}, \theta_i$) switching between four states (A,B,C,D) via E. c, Size definition of 1/4 unit (three patterns as examples). d, The folding/cutting pattern of one ring-like unit with four 1/4 units (yellow triangles: connecting panels; green dots: cycle points). e, Size definition of ring-like unit. f, Contraction of ring-like unit and 2D tessellation with 3 × 3 units. g, 16 patterns of a 1/4 unit with four bits and five kinds of deformations (orange, brown, red, gray, and blue, see right plot) in Y direction and one deformation in X direction. h, Assemble of a ring-like unit with 12 bits and 12 $\gamma$-shaped memory alloy sheets (outward: state '1'; inward: state '0'), and experimental setup (heat platform, camera) for measuring sample thermal deformations. For samples, $\alpha = 90°$, $\beta = 60°$, $q = n = m = 15$ mm . (For interpretation of the references to color in this figure legend, the reader is referred to the web version of this article.)

with large tunable thermal expansion properties, the minimum and maximum value of thermal expansion coefficient of the 2D ring-like structure coupled with SMA patches are $\sim -8 \times 10^{-3}$ K$^{-1}$ and $\sim 2 \times 10^{-3}$ K$^{-1}$ (see Supplementary Materials for calculation), which are ∼10 and ∼2 times of the 2D mechanical metamaterials [30], respectively. Beyond this, we can expect even larger deformation range by increasing the value of plane angle $\beta$ (see Fig. S6A, here $\alpha = 90°, \beta = 60°$ for easy fabrication) and optimizing the SMA patches.

The strain is measured with the help of imaging processing method based on the deformation images/videos, as this method provides non-contact measurements on the deformation of the sample. We calibrated the overall system and obtained the ratio of the structures' real size to pixel (0.073 mm/pixel). The temperature (marked in Figs. 2 and 3) was measured with thermocouple from the SMA sheet, which is the key part with local thermal-coupled deformation mechanism (see Fig. S7). The thermal expansion coefficient of the ring-like structure with $N =$ 1 in 2D isotropic pattern influenced by the geometric parameters is also shown in Fig. S7.

## 3. 3D coded thermal expansions

Further, a 3D cubic unit can be formed by symmetrically combining four ring-like structures (Fig. 4a, the two transparent planes denote the symmetrical planes). With such 3D cubic units, we can create 3D cellular structures and obtain both isotropic and anisotropic deformation property. Fig. 4b shows the isotropic contraction process (from state #A to #C) of a 3D cellular structure with 4 × 4 × 4 3D cubic units. The 3D unit in state #C (red) within the one in state #A (gray) shows near 7/8 contraction of the original volume. Fig. 4c shows the deformation photographs of a cubic unit actuated by SMA sheets during heat with different temperatures, strains and times. Moreover, the cubic unit can also be independently coded along X, Y and Z direction, which exhibits anisotropic deformation property. Fig. 4d shows that four

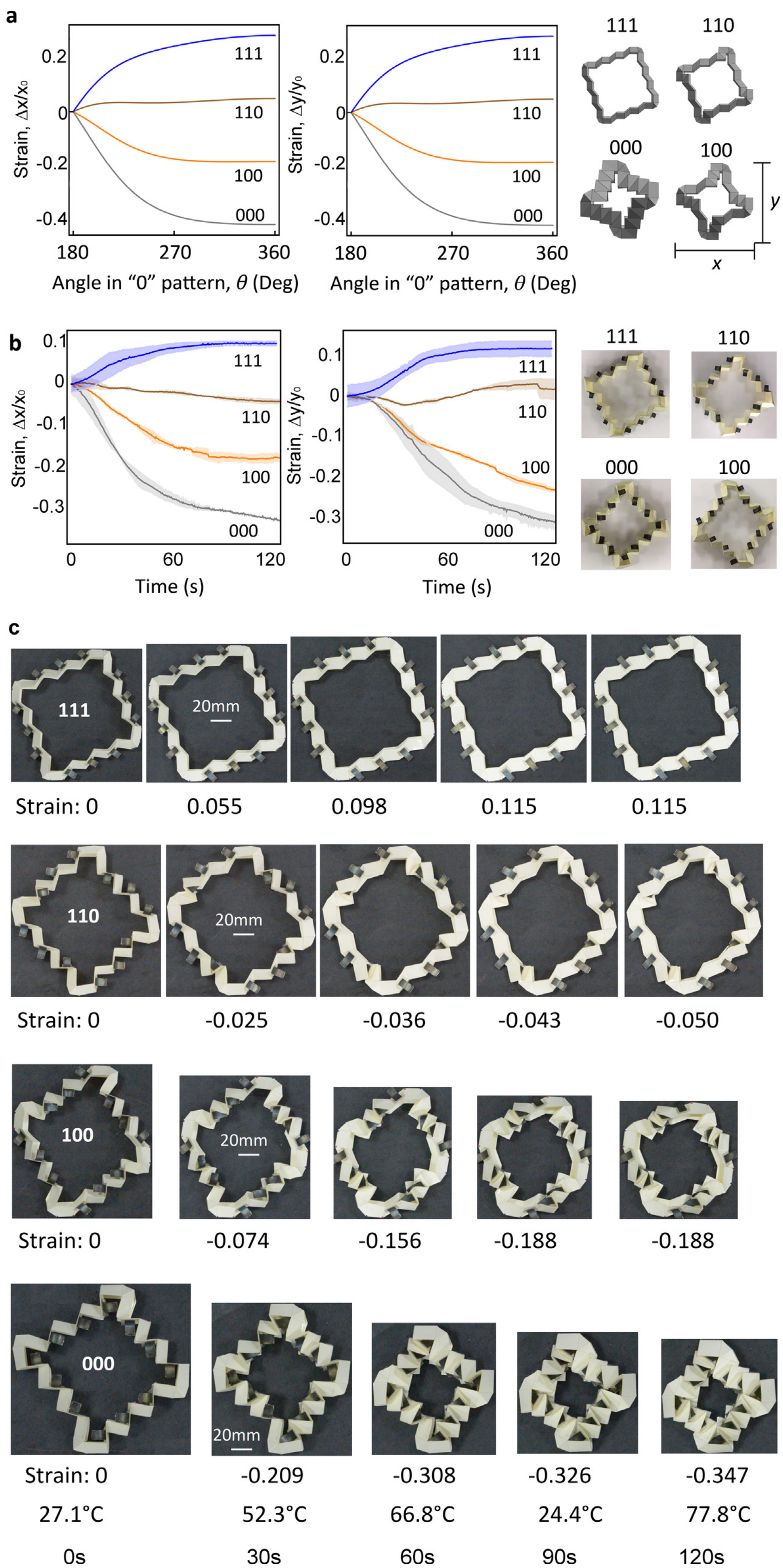


**Fig. 2.** Isotropic thermal deformation of 2D unit. a, Simulations of the strains $\Delta x/x_0$ and $\Delta y/y_0$ as functions of $\theta$, each ring-like unit consists of 1/4 units with the same pattern (111, 110, 100, and 000). b, Measurements of the strains of those unit patterns on the heat platform as functions of heat time. c, Isotropic deformation photographs at heating time 0s, 30 s, 60 s, 90 s, and 120 s with the corresponding temperatures of SMA patch and structure strains. Curve, mean value of measurement; shading, one standard deviation. $\Delta x/x_0 = x/x_0 - 1$, where $x$ and $x_0$ denote the instantaneous size and initial size with $\theta = 180°$ in X direction, respectively. Similarly, $\Delta y/y_0 = y/y_0 - 1$.

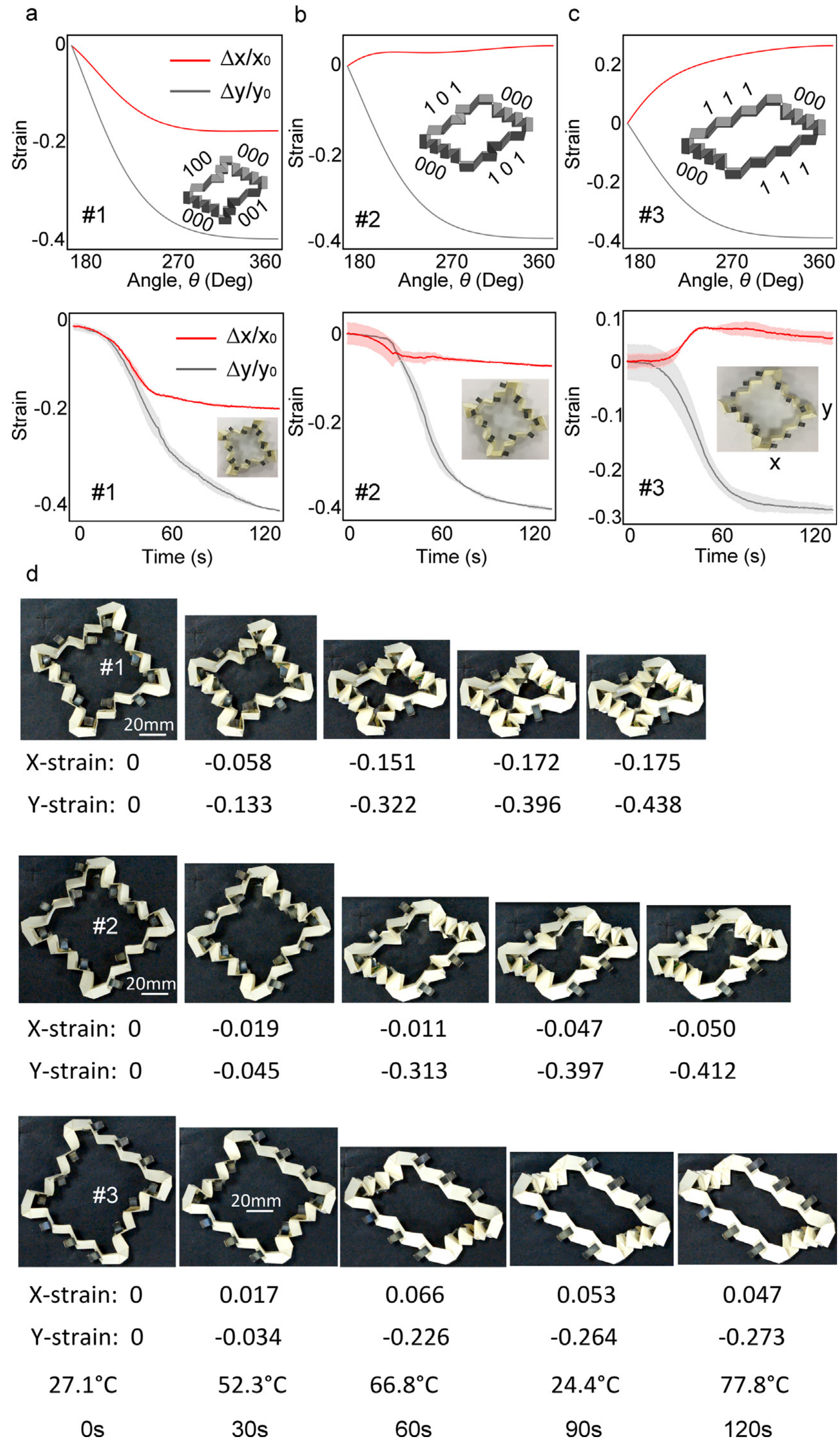


**Fig. 3.** Anisotropic thermal deformation of 2D unit. The simulations and measurements of the strains $\Delta x/x_0$ (red curve) and $\Delta y/y_0$ (gray curve) for a, Pattern #1 (100-000-100-000), b, Pattern #2 (101-000-101-000), c, Pattern #3 (111-000-111-000), d, Anisotropic deformation photographs at heating time 0s, 30 s, 60 s, 90 s, and 120 s with the corresponding temperatures of SMA patch and structure strains. Curve, mean value of measurement; shading, one standard deviation . (For interpretation of the references to color in this figure legend, the reader is referred to the web version of this article.)

quarter units (strips highlighted in orange) along X direction can be coded as 111, 011, 001 and 000, and other strips along Y and Z direction are unchanged. The same method can be used to independently code the 3D unit along Y direction (Fig. 4e), thus here we only show the results of X direction coding (Fig. 4g). But it is different for Z direction coding, where eight strips need to be coded (see Fig. 4f for the eight orange strips, see Fig. 4h for deformation results). Nevertheless, we can observe independent reprogrammable deformation behaviors along each direction. In Fig. 4g, with X-direction coding four X-strains (pink lines with four line types for four modes #1, #2, #3 and #4 in Fig. 4d) can be generated, while Y-stain (green) and Z-strain (blue) have only one deformation behavior, individually. Likewise, with Z-direction coding four Z-strains (blue with four line types for #1, #2, #3 and #4 in Fig. 4f) are shown in Fig. 4h, while Y-stain (green) and X-strain (pink) have only one deformation behavior, respectively. See Fig. 4i–k for the detailed deformation processes of coding the cubic unit in modes #1, #2, #3 and #4 along

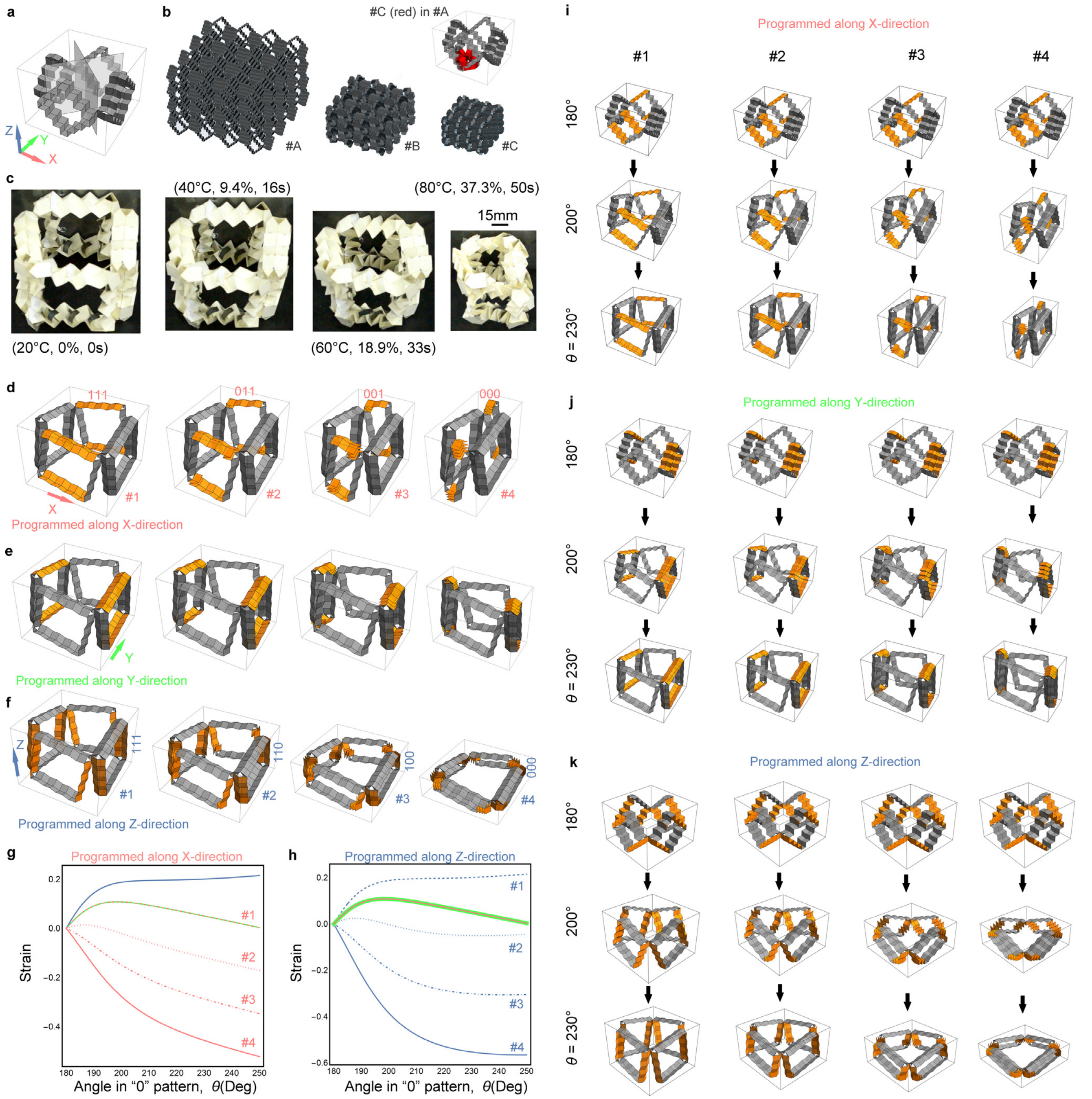


**Fig. 4.** Coded deformations in three directions. a, 3D cubic unit built by four ring-like units according to two symmetrical planes. b, Isotropic contraction of cellular structure with $4 \times 4 \times 4$ cubic units with $\theta = 180°$ (#A), $\theta = 210°$ (#B), $\theta = 250°$ (#C). The insert shows #C state unit (red) in #A state unit (gray) to compare the sizes. c, Deformation of a cubic unit sample with various temperatures, strains and heat times. Cubic unit independently coded along d, X-direction (programming the four orange strips along X-direction for #1, #2, #3, and #4 mode), e, Y-direction (programming the four orange strips along Y-direction for #1, #2, #3, and #4 mode), f, Z-direction (programming the eight orange strips along Z-direction for #1, #2, #3, and #4 mode). Strain $-\theta$ curves in the four modes when the cubic unit is independently coded along g, X-direction, h, Z-direction (the green line is widened to make the pink line visible). Detailed cubic unit coding along i, X, j, Y, and k, Z direction. Color rule: pink, green, and blue denote X, Y, and Z direction, respectively. Here $\alpha = 90°$, $\beta = 80°$ . (For interpretation of the references to color in this figure legend, the reader is referred to the web version of this article.)

the three directions. See also Supplementary Videos 9∼11 for isotropic and anisotropic deformation of a 3D unit with $4 \times 4$ bits.

The heating platform generates a temperature gradient. For 2D structure, this effect is negligible, but for 3D structure, the temperature gradient may lead to inhomogeneous heating. Therefore, here we focus on geometric simulation of strain (Fig. 4g and h) for the 3D case due to the limitation of our experimental devices. In the future, we are planning build a new system with proper-sized oven to provide more accurate heating and temperature-deformation measurements.

## 4. Relation between thermal expansion property and Poisson's ratio

For the ring-like units, the thermal expansion property is positively correlated with its Poisson's ratio. Fig. 5a shows that an initial ring-like structure (the simplest case with one bit for

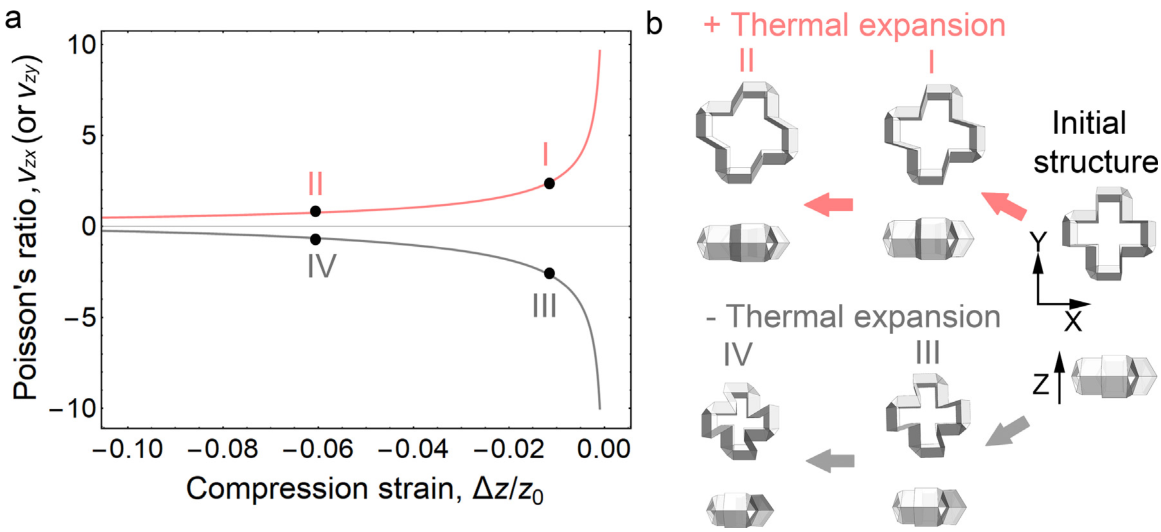


**Fig. 5.** Relation between thermal expansion and Poisson's ratio for ring-like structure. a, Poisson's ratio, $\nu_{zx}$ (or $\nu_{zy}$), as a function of compression strain, $\Delta z/z_0$ ($\nu_{zx} > 0$: pink curve, I and II; $\nu_{zx} < 0$: gray curve, III and IV). b, Two paths of thermal deformations (expansion: pink arrows, I and II; contraction: gray arrows, III and IV). . (For interpretation of the references to color in this figure legend, the reader is referred to the web version of this article.)

each quarter unit) can be coded into two paths of deformations. On one hand, a structure in '+' thermal expansion mode along X- and Y- direction by setting every bit as '1' state (see Fig. 5b I and II for the two reconfigurations under compression, also the two reconfigurations during heat) possesses '+' Poisson's ratio, $\nu_{zx}$ and $\nu_{zy}$ (see Fig. 5a I and II, pink curve). On the other hand, a structure in '−' thermal expansion mode by setting every bit as '0' state shows '−' Poisson's ratio (see Fig. 5a and b, III and IV, gray curve). The thermal deformations of a ring-like structure with multi-bit in experiment can be seen in Fig. 2b and c (pattern '111', '+' thermal expansion; pattern '000', '−' thermal expansion). However, if this positively correlated relation can be applied for other materials is an open question. Here, compression strain is defined as $\Delta z/z_0 = z/z_0 - 1$, where $z$ and $z_0$ denote the instantaneous Z-size and initial Z-size with $\theta = 180°$, respectively. Poisson's ratio is calculated by $\nu_{zx} = -\frac{dx/x}{dz/z}$, $\nu_{zy} = -\frac{dy/y}{dz/z}$ [31].

As a limitation of this work, the structures are fabricated using thick paper, which is bendable, resulting in difficulties of accurately controlling the metamaterial's overall deformation. In the future, we are planning that the structures can be fabricated by stiffer plastic or metal facets with hinges by using 3D printing techniques and coupled with SMA sheets. Also, finite element analysis will be used to simulate the entire deformation process for better demonstrations on the local and global effects of the SMA patches and the kirigami structures, respectively. Last, the shape of the SMA patch needs to be optimized, which is expected to enhance the coupling and result in better overall performance of the kirigami metamaterial.

In summary, we have demonstrated that a kirigami-inspired ring-like microstructure provides a new building brick for designing artificial materials with coded thermal expansion properties that support targeted isotropic and anisotropic deformations upon outside temperature changes. By conducting both numerical and experimental studies, we show that the thermal deformations of such metamaterials can be tuned not only by changing the geometrical elements (angles or lengths) but also by varying the binary codes encrypted in the microstructures, which provides a new dimension for tunable metamaterial designs. Moreover, we find that there is a positively correlated relation between coded thermal expansion property and Poisson's ratio. Although paper-made structures in centimeter scale are investigated here, our design strategy is able to be potentially extended to numerous engineering materials and demanded scales, which opens up avenues for designing new smart structures and novel devices in the fields of energy, optics, aerospace, and electronics.

## Declaration of competing interest

The authors declare that they have no known competing financial interests or personal relationships that could have appeared to influence the work reported in this paper.

## Data and code availability

The data shown in the figures and the code supporting the findings of this study are available from the corresponding author on request.

## Acknowledgments

N.Y. acknowledges the National Natural Science Foundation of China (No. 11872046), Tianjin Science Key Funding (14JCZDJC39500, 18JCZDJC10030), the Scientific Research Funding of Shantou University, China (NTF19012), and 2020 LKSF Cross-Disciplinary Research Projects, China (2020LKSFG01D). R.Z. acknowledges the National Natural Science Foundation of China (No. 11872112, No. U1837602), and the start-up funding of Beijing Institute of Technology, China (No. 2018CX01031).

## Appendix A. Supplementary data

Supplementary material related to this article can be found online at https://doi.org/10.1016/j.eml.2020.100912.

## References

[1] N. Yamamoto, E. Gdoutos, R. Toda, V. White, H. Manohara, C. Daraio, Thin films with ultra-low thermal expansion, Adv. Mater. 26 (2014) 3076.
[2] K. Takenaka, Negative thermal expansion materials: technological key for control of thermal expansion, Sci. Technol. Adv. Mater. 13 (2012) 013001.
[3] M.M. Toropova. C. A. Steeves, Adaptive bimaterial lattices to mitigate thermal expansion mismatch stresses in satellite structures, Acta Astronaut. 113 (2015) 132.
[4] W. Miller, C.W. Smith, D.S. Mackenzie, K.E. Evans, Negative thermal expansion, J. Mater. Sci. 44 (2009) 5441.
[5] K.L. Chopra, P.D. Paulson, V. Dutta, Thin-film solar cells, Prog. Photovolt.: Res. Appl. 12 (2004) 69.

[6] M. Kanik, S. Orguc, G. Varnavides, J. Kim, T. Benavides, D. Gonzalez, T. Akintilo, C.C. Tasan, A.P. Chandrakasan, Y. Fink, P. Anikeeva, Strain-programmable fiber-based artificial muscle, Science 365 (2019) 145.
[7] K. Takenaka, Y. Okamoto, T. Shinoda, N. Katayama, Y. Sakai, Colossal negative thermal expansion in reduced layered ruthenate, Nat. comm. 8 (2017) 14102.
[8] A.W. Sleight, Compounds that contract on heating, Inorg. Chem. 37 (1998) 2854.
[9] C.N. Chu, N. Saka, N.P. Suh, Negative thermal expansion ceramics, Mater. Sci. Eng. 95 (1987) 303.
[10] G.D. Barrera, J.A.O. Bruno, T.H.K. Barron, N.L. Allan, Negative thermal expansion, J. Phy.: Condens. Matter 17 (2005) R217.
[11] E. Boatti, N. Vasios, K. Bertoldi, Origami metamaterials for tunable thermal expansion, Adv. Mater. 29 (2017) 1700360.
[12] F. Pan, Y. Li, Z. Li, J. Yang, B. Liu, Y. Chen, 3D pixel mechanical metamaterials, Adv. Mater. 31 (2019) 1900548.
[13] T. Frenzel, M. Kadic, M. Wegener, Three-dimensional mechanical metamaterials with a twist, Science 358 (2017) 1072.
[14] J.J. Lehman, R.S. Lakes, Strong Stiff, Zero thermal expansion lattices via material hierarchy, Compos. Struct. 107 (2014) 654.
[15] T.-C. Lim, Anisotropic and negative thermal expansion behavior in a cellular microstructure, J. Mater Sci. 40 (2005) 3275.
[16] J. Qi, J.W. Halloran, Negative thermal expansion artificial material from iron-nickel alloys by oxide co-extrusion with reductive sintering, Mater. Sci. 39 (2004) 4113.
[17] H. Xu, D. Pasini, Structurally efficient three-dimensional metamaterials with controllable thermal expansion, Sci. Rep. 6 (2016) 34924.
[18] E. Gdoutos, A.A. Shapiro, C. Daraio, Thin and thermally stable periodic metastructures, Exp. Mech. 53 (2013) 1735.
[19] Q. Wang, J.A. Jackson, Q. Ge, J.B. Hopkins, C.M. Spadaccini, N.X. Fang, Lightweight mechanical metamaterials with tunable negative thermal expansion, Phys. Rev. Lett. 117 (2016) 175901.
[20] C.A. Steeves, S.L. dos Santos e Lucato, M. He, E. Antinucci, J.W. Hutchinson, A.G. Evans, Structurally robust materials that combine low thermal expansion with high stiffness, J. Mech. Phys. 55 (2007) 1803.
[21] R. Lakes, Cellular solid structures with unbounded thermal expansion, J. Mater. Sci. Lett. 15 (1996) 475.
[22] J. Qu, M. Kadic, A. Naber, M. Wegener, Micro-structured two-component 3D metamaterials with negative thermal-expansion coefficient from positive constituents, Sci. Rep. 7 (2017) 40643.
[23] Z.Y. Wei, Z.V. Guo, L. Dudte, H.Y. Liang, L. Mahadevan, Geometric mechanics of periodic pleated origami, Phys. Rev. Lett. 110 (2013) 215501.
[24] C. Lv, D. Krishnaraju, G. Konjevod, H. Yu, H. Jiang, Origami based mechanical metamaterials, Sci. Rep. 4 (2014) 5979.
[25] M. Schenk, S.D. Guest, Geometry of miura-folded metamaterials, Proc. Natl. Acad. Sci. USA 110 (2013) 3276.
[26] S. Li, H. Fang, K.W. Wang, Recoverable and programmable collapse from folding pressurized origami cellular solids, Phys. Rev. Lett. 117 (2016) 114301.
[27] L.H. Dudte, E. Vouga, T. Tachi, L. Mahadevan, Programming curvature using origami tessellations, Nature Mater. 15 (2016) 583.
[28] J.L. Silverberg, A.A. Evans, L. Mcleod, R.C. Hayward, T. Hull, C.D. Santangelo, I. Cohen, Using origami design principles to fold reprogrammable mechanical metamaterials, Sci. 345 (2014) 647.
[29] J.L. Silverberg, J.-H. Na, A.A. Evans, B. Liu, T.C. Hull, C.D. Santangelo, R.J. Lang, R.C. Hayward, I. Cohen, Origami structures with a critical transition to bistability arising from hidden degrees of freedom, Nature Mater. 14 (2015) 389.
[30] X. Ni, X. Guo, J. Li, Y. Huang, Y. Zhang, J.A. Rogers, 2d mechanical metamaterials with widely tunable unusual modes of thermal expansion, Adv. Mater. 31 (2019) 1905405.
[31] H. Yasuda, J. Yang, Reentrant origami-based metamaterials with negative Poisson's ratio and bistability, Phys. Rev. Lett. 114 (2015) 185502.